ELSEVIER

Contents lists available at ScienceDirect

Ceramics International

journal homepage: www.elsevier.com/locate/ceramint





Reacting Mn₃O₄ powders with quaternary ammonium hydroxides to form two-dimensional birnessite flakes

Mary Qin Hassig ^a, Takayuki Kono ^b, Michael Carey ^c, Kaustubh Sudhakar ^a, Gregory R. Schwenk ^a, Hussein O. Badr ^a, Michel W. Barsoum ^{a,*}

- ^a Department of Material Science and Engineering, Drexel University, Philadelphia, PA, USA
- ^b Murata Manufacturing Co., Ltd, Nagaokakyo-shi, Kyoto, Japan
- ^c Riverside Research, Air Force Research Laboratory, Wright Patterson Air Force Base, Dayton, OH, USA

ARTICLE INFO

Handling Editor: Dr P. Vincenzini

Keywords:
D. Transition metal oxides
A. Films
Two-dimensional materials
Band gap
Oxygen evolution reactions

ABSTRACT

There is a current interest in synthesis of two-dimensional (2D) materials that would be cost-efficient to scale to industry production. In this study, we report on a bottom-up approach to convert a manganese oxide (Mn₃O₄) powder into crystalline, 2D layered birnessite flakes. The Mn₃O₄ precursor powder, is reacted with aqueous solutions of, tetramethyl-, tetraethyl- or tetrabutylammonium hydroxide in a shaker oven at 80 °C for 4 days. X-ray diffraction confirmed that in all cases, upon filtration of colloidal suspensions, well-stacked, crystalline, 2D MnO₂ birnessite layers formed, that upon characterization were found to be quite similar. The major differences were the spacings between the flakes that depended on cation size. Selected area diffraction patterns in a transmission electron microscope confirmed both the structure and the polycrystallinity of the flakes. Raman spectroscopy confirmed the structure. The zeta-potentials of the 2D flakes were measured to be \approx -35 \pm 2 mV. When UV–Vis spectra were converted to Tauc plots, direct and indirect band gap energies of \approx 2.15 and \approx 2.60 eV were obtained, respectively. Additionally, the oxygen evolution reactivity of our birnessite flakes significantly are better than those found for Pt/C, demonstrating a high degree of catalytic reversibility. The facile conversion of a relatively inexpensive, earth-abundant oxide, Mn₃O₄, into a highly value-added 2D birnessite using a one-pot, simple hugely scalable, protocol at near ambient temperatures and pressures with various quats can be considered a breakthrough in the production of these nanomaterials.

1. Introduction

With uses in lithium-ion batteries [1,2], water oxidation catalysis, in development of solar cells [3–5], molecular absorption [5–7], and some biological applications including biosensing and drug delivery [8], manganese (Mn) oxides have been thoroughly explored in recent years. Manganese oxide exists in many structures including manganosite, hausmannite, partridgeite, and cryptomelane [9]. It is found naturally in ocean nodules and soil coatings, mainly [3]. For this project we are focused on synthesizing 2D, layered manganese oxide, also known as, birnessite or δ -MnO $_2$ [9]. The name comes from Birness, Scotland, where a natural deposit of this material was found [10]. In nature, birnessite is poorly crystalline [3].

Multilayer (ML) δ -MnO₂ is typically synthesized through one of several top-down synthesis routes such as the oxidation of a manganous hydroxide with O₂ or Cl₂ in a hydroxide solution [9,11], the reduction of

potassium permanganate (KMnO₄) [5,9,12], or the hydrothermal treatment of manganese compounds [11,13]. Kai et al. were the first to obtain single/few layered birnessite, using a co-precipitation method. The group used a mixture of hydrogen peroxide and tetramethy-lammonium hydroxide (TMAH) or tetrabutylammonium hydroxide (TBAH) in combination with an aqueous solution of manganese (II) chloride (MnCl₂) to obtain a colloidal suspension of monolayer $\delta\text{-MnO}_2$

Another way to synthesize single layer δ -MnO $_2$ is to use a top-down approach starting with a layered protonic Mn-oxide precursor. As the precursor is exfoliated, using a TBAH solution, the TBA $^+$ cations intercalate between the layers and result in their delamination [15,16]. Another method is to start with a layered precursor, then use acid leaching with HCl to create a protonated form, that is then shaken in a TBAH solution to exfoliate and delaminate the layers. Samples are then washed with water to remove excess TBAH and configured to separate

^{*} Corresponding author. LeBow 444, 3141 Chestnut Street, Philadelphia, PA 19104 E-mail address: barsoumw@drexel.edu (M.W. Barsoum).

the single layer from the MLs [17-19]. This can also be done via sonication [20].

Recently, we showed that reacting a number of water insoluble Mn compounds - including $\rm Mn_3O_4,\,Mn_2O_3,\,MnB,\,Mn_5SiB_2,\,$ and $\rm Mn_2AlB_2$ - with 25 wt% aqueous solution of TMAH resulted in formation of relatively large crystalline, $\delta\text{-MnO}_2$ flakes. This work was inspired by our previous work which was performed on binary and ternary Ti compounds including TiB_2, TiC, and TiN, and the MAX phases, to obtain titania-based lepidocrocite one dimensional, 1D, nanofilaments (NFs). The NFs can self-assemble into larger quasi-2D structures that resemble flakes in some cases [21,22]. As discussed in our original work, the bottom-up method described here is less expensive and time consuming, and more easily scalable than the top-down methods mentioned above [23]. This method would be most valuable in areas where large quantities of birnessite are needed, such as water filtration to remove radioactive elements [24], and/or organic pollutants [25].

In alignment with our previous work, part of this work's purpose was to validate the ability to synthesize $\delta\text{-MnO}_2$ with other quaternary ammonium hydroxide (quat) aqueous solutions [23]. The samples were processed in a manner similar to that outlined in our first paper. In short, we mixed Mn_3O_4 powders with TMAH for 4 d at 80 °C. Herein the chosen precursor was again Mn_3O_4 because it is relatively inexpensive, earth abundant and non-toxic [26–28]. Like in our previous work, we maintained the molar ratio of Mn to the quat cation constant at 0.47. The materials produced are crystalline, birnessite 2D flakes. In this paper, they will be referred to as quat-derived birnessite (QDB).

Another driving force behind this work was to establish whether it is possible to synthesize the same material with a less hazardous quat than TMAH, that is known to be a hazardous chemical with serious health repercussions if handled improperly. TMAH is fatal if swallowed (at a concentration of 16.67 mg/kg) or in contact with skin. It can cause serious eye damage, damage to the central nervous system after one exposure, and damage to the liver and thymus with repeated exposure. It is also listed as an aquatic hazard, both acute and chronic [29,30]. TBAH does not come without risks, like TMAH, but it can also cause serious eye damage, and can be fatal if swallowed, but at much higher concentrations (2.5 g/kg). However, it is only a skin sensitizer, meaning it could cause allergic skin reactions, but does not target specific organs in terms of toxicity, in single or long-term exposure [31,32]. Tetraethylammonium hydroxide (TEAH) was chosen less because of safety, as it is known to cause nervous system, eye, and thymus damage, but more because it has an alkyl chain length between TMAH and TBAH. A secondary goal of this work was to assess the length of the alkyl chain on structure and properties.

2. Material and methods

2.1. Sample processing

Synthesis of our birnessite flakes involved immersing Mn_3O_4 powder [Mn (II, III) oxide, 97%, Strem Chemicals] in a quat solution. The latter was an aqueous solution of 25 wt% TMAH [Electronic Grade, Thermo ScientificTM], 40 wt% TBAH [Thermo ScientificTM], or 35 wt% TEAH [Thermo ScientificTM]. A molar ratio of 0.47:1 of Mn to quat cation, respectively, was maintained. This ratio was typically accomplished using 1 g Mn₃O₄ powder and 10 mL of TMAH, 11.5 mL of TEAH or 18 mL of TBAH, to form a mixture. The latter was placed in a high-density polyethylene bottle at 80 °C in a shaker oven and shaken at approximately 200 rpm for 4 d.

After reaction, a dark brown product with a viscosity akin to water, was collected and washed. The initial washing step involves rinsing the sample with 200 proof ethanol (EtOH) [Decon Labs Inc.] and centrifuging the sample at 5000 rpm for 10 min and discarding the supernatant. This step helps remove any residual quats from the samples. This process was repeated-until the supernatant pH after washing was ≈ 7 or 8, which typically took about 4 washes. The samples were then

redispersed in deionized (DI) water by shaking the centrifuge tube on a vortex stirrer and centrifuged again at 3500 rpm for 30 min with no stirring or sonication. In this case the colloidal suspension was collected. The final step was to filter the colloidal suspension using a vacuum filtration system, using Celgard as a filtration membrane to obtain filtered films (FFs) that were then characterized. The filtering typically took 12–24 h.

2.2. Characterization methods

2.2.1. X-ray diffraction (XRD)

An X-ray diffractometer, XRD (Rigaku MiniFlex) operated with Cu $K\alpha$ radiation was used to obtain XRD patterns of dried powders. The samples were scanned between 2° and 65° 2θ range using a step size of 0.02° and dwell time of 0.4 s per step.

2.2.2. Scanning electron microscope (SEM)

Micrographs were obtained using an SEM (Zeiss Supra 50 V P, Carl Zeiss SMT AG, Oberkochen, Germany). The settings were set to a type II secondary electron detector, a 30 μm aperture, a working distance between ≈ 8 and 10 mm, and an accelerating voltage of 2 kV.

2.2.3. Transmission electron microscope (TEM)

TEM imaging and selected electron diffraction (SAED) patterns were collected using a field-emmision TEM (JEOL F200). The TEM was operated at 200 keV. Images and diffraction patterns were collected on camera (Gatan OneView IS). Samples were prepared by first diluting the colloidal suspension, then drop casting a few drops on a carbon-coated, lacey-carbon, copper TEM grid.

2.2.4. Raman spectroscopy (RS)

Raman scattering spectra were collected at room temperature (RT) in air. Measurements were done with an inverted reflection mode on a spectrometer (Renishaw InVia, Gloucestershire, U.K.) equipped with 63 \times (NA = 0.7) objectives and a diffraction-based RT CCD spectrometer. Ar laser (514 nm) was used, and the power of the lasers was kept in the \sim 0.1–0.5 mW range.

2.2.5. Zeta potential

A zetasizer (Nano-ZS, Malvern Panalytical, Malvern) was used for the electrophoretic mobility measurements. The electrophoretic mobility values converted to zeta potentials, ζ , using the Smoluchowski model. All measurements were carried out at ambient conditions, with a holding equilibrium time of 120 s. The concentration during these measurements was 0.1 wt%.

2.2.6. X-ray photoelectron spectroscopy (XPS)

An XPS spectrometer (VersaProbe 5000 (Physical Electronics, Chanhassen, MN) was used to obtain XPS spectra. Monochromatic Al-Ka X-rays with a pass energy of 23.5 eV, a step size of 0.05 eV, and a spot size of 200 μm was used to irradiate the sample surface. Samples were mounted on the XPS stage using carbon tape. CasaXPS v.2.3.21PR1.0 software was used for peak fitting and chemical-composition analysis with a Shirley background. The obtained spectra were calibrated by setting the C–C peak to 285.0 eV.

2.2.7. Gas sorption

Gas sorption analysis was carried out using a Quantachrome Autosorb iQ with nitrogen (N_2) adsorbates. Prior to the analysis, the samples were outgassed under vacuum at 60 °C for 1 h, 100 °C for 1 h, 150 °C for 12 h. The specific surface area (SSA) was calculated from the volume absorbed at 77 K using the Brunauer-Emmet-Teller (BET) equation. The gas sorption measurements were carried out on a powder obtained by manually crushing the FF in a mortar and pestle.

2.2.8. Ultraviolet-visible spectroscopy (UV-vis)

The UV–vis data were collected using a spectrophotometer (Cary 60, Agilent Technologies, Inc., Santa Clara, CA). The data were collected at intervals of 0.5 nm and a scan rate of 300 nm/min. The measurements were made on dispersed colloids in quartz cuvettes. These colloids were prepared by creating a 1% dilution of the colloid after washing with DI $_{12}$ O.

2.2.9. Electrochemical measurement - oxygen evolution reaction (OER)

A fluorinated ethylene propylene (FEP) electrolytic cell was prepared by successive boiling and washing with Millipore water (18.2 m Ω -cm, <3 ppb total organic content). The catalyst ink was prepared by dispersing 4.5 mg of the Mn-based catalyst and 4.5 mg carbon black (Vulcan XC-72 R) in 2 mL of isopropyl alchohol, IPA (99.99%, Sigma). Then, 5 μL of an alcohol based 5 wt NafionTM dispersion (Ion Power) was added as a dispersing agent and the ink was bath sonicated for 25 min. During this time, a glassy carbon substrate disk (Sigradur G HTW), with a diameter of 0.196 cm, was polished with alumina powder, rinsed with Millipore water, and prepared for catalyst loading. Approximately 8 µL (delivered in 2 increments of 4 µL each) of the catalyst ink were loaded onto the glassy carbon substrates and dried under a gentle flow of Ar to afford catalyst films. Oxygen evolution reaction (OER) measurements were performed while bubbling O2 through a 0.1 M potassium hydroxide (KOH) (from pellets 99.99%, metal basis, Sigma) electrolyte solution by applying a potential using a potentiostat (Autolab 302 N) from -0.8 V to 0.9 V with respect to reversible hydrogen electrode (RHE) with a rotating disc electrode, RDE (Pine Instruments), set to 1600 RPM.

3. Results and discussion

A schematic of our process can be found in Fig. 1. As noted above, a 0.47 M ratio between Mn and the quat cation was maintained. This choice was made so that our results can be compared to our previous work [23]. It is worth noting that these conditions are far from optimized or accelerated. After washing the resulting product with EtOH, until pH \approx 7, the samples were dispersed in DI water at which point they formed stable colloidal suspensions, which were then vacuum filtered to make FFs, an example of which can be seen on the right-hand side of Fig. 1.

3.1. XRD

The QDB FFs are free-standing, flexible, and dark brown, almost black in color. The XRD patterns, on a log scale, obtained on FFs using TMAH, TEAH and TBAH, are, respectively, plotted in black, blue, and red in Fig. 2. These patterns are typical of 2D materials and can be characterized by their 00L reflections; 6 for TMAH, 6 for TEAH and 8 for the TBAH FFs. These patterns imply that order along the stacking direction, viz. the c-axis, is quite high. As importantly the interlayer spacing, *d*, calculated from these peaks are 9.4 Å for TMAH, 9.4 Å for TEAH and 12.1 Å TBAH. The 9.4 Å value for TMAH not only agrees with

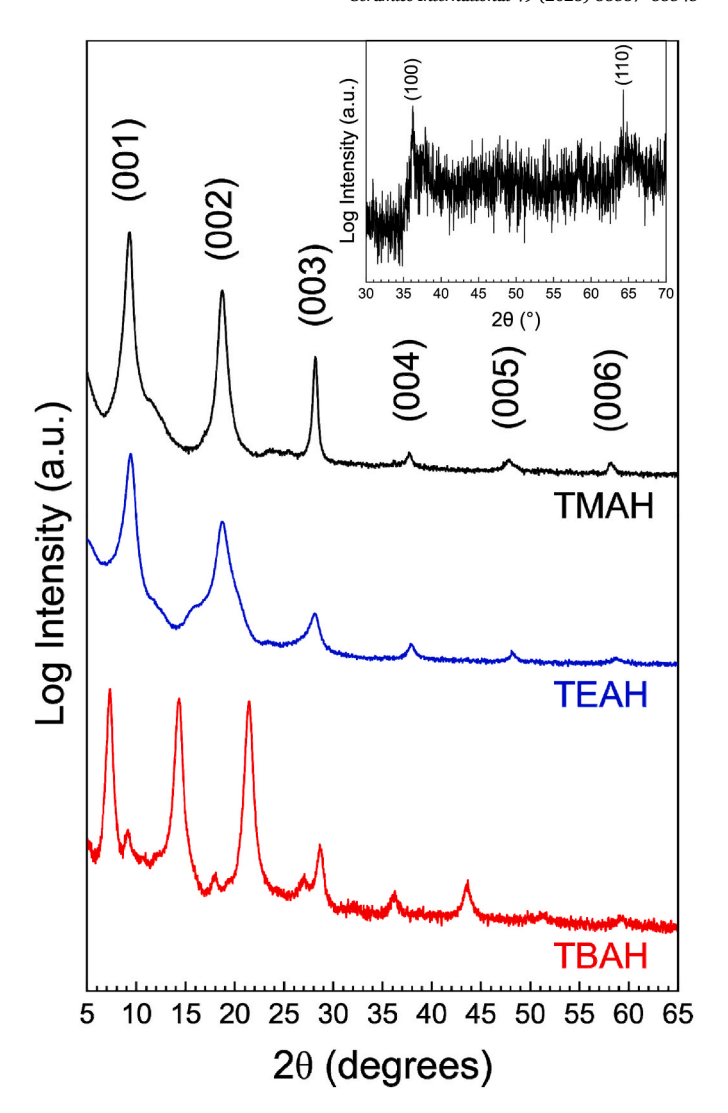


Fig. 2. X-ray diffractograms, on log scale, of QDB FFs made with TMAH (black), TEAH (blue) and TBAH (red). Inset shows XRD pattern of TMAH in 30to 70 2 θ range. (For interpretation of the references to color in this figure legend, the reader is referred to the Web version of this article.)

our previous findings [23], but with other TMA⁺ intercalated birnessite studies in the literature [14,33,34]. The \approx 9.4 Å, *d*-value for TEA⁺ is again consistent with literature values for TEA⁺ intercalated samples [35]. Lastly, the 12.1 Å value for TBA⁺ is also consistent with interlayer spacing for TBA⁺ intercalated birnessite [15,35,36].

To check the reasonableness of these d-spacings, and gain more insight into the structure of what lies in between the layers, we estimated the diameters of the hydrated cations as follows. Assuming the

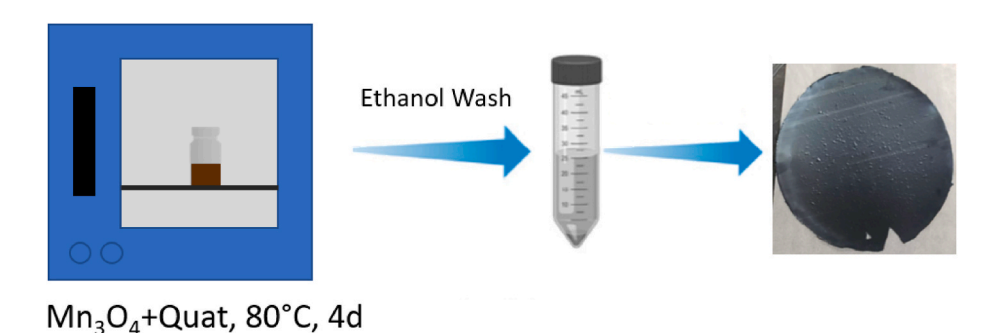


Fig. 1. Schematic of fabrication process.

values listed in Table 1 for the various quat cations [37,38] and the thickness of a single MnO₂ slab to be 1.9 Å [23], it follows that the thicknesses of the hydration shells surrounding these cations are ≈ 1.7 Å, ≈ 0.6 Å and ≈ 1.94 Å, respectively.

Since these values are all positive, but < 2.8 Å diameter of a water molecule [39,40], it follows that the latter must be ordered and arranged in such a way as to fit in the interstitial spaces between the C-chains of the alkyl group and the oxygen atoms of the birnessite. Based on these values, we sketched the interlayer space for each quat (Fig. 3). Given the uncertainty in the values of some of our input values - mostly the cationic radii, and the small distance between cation and MnO2 slabs in the case of TEA⁺, herein we assume that there is *no* water between it and the slabs (Fig. 3b). In contradistinction, for the other two cations, we assume that the water molecules are partially embedded in the quat cations as shown in Fig. 3a and c. Said otherwise, the situation for the TMA⁺ and TBA⁺ are comparable. At this juncture it is unclear why the TEA⁺ cation behaves differently than the other two. We note in passing that based on the TEA+ results the maximum diameter of this cation must be very close to the one we chose, viz. 6.74 Å. Table 1 also compares our results with those of Brock et al. [1]. It is important to note that Brock et al. assumed the MnO₂ slabs are 4.5 Å thick.

Like in our previous work [23], we were unable to distinguish the non-basal birnessite XRD reflections in any of the QDB FFs patterns because of the good stacking. However, a powder XRD pattern of a TMAH-derived material (inset in Fig. 2) indeed show the non-basal (100) and (110) peaks, at d-spacings of d_{100} 2.49 Å and $d_{110}\approx 1.43$ Å, respectively. Drits et al. reported d_{100} and d_{110} to be 2.42 Å and 1.42 Å, respectively – and ascribed them as characteristic peaks of turbostatic 2D birnessite [41]. In our previous work, we reported $d_{100}\approx 2.48$ Å and $d_{110}\approx 1.44$ Å. In short, the three studies match each other well.

And while the resulting materials are quite similar, the reaction rates are different. After 4 d TMAH has the highest yield of \approx 60%, followed by TEAH with a yield of \approx 50%, with TBAH being \approx 15%. The colloidal concentrations are also quite different with TMAH being 3.44 g/L, TEAH being 1.5 g/L, TBAH being 0.24 g/L when 30 mL of water is added to the washed sediment of 1 g of precursor. As we are in control of the amount of water added to create the colloids, the colloid concentration can be higher or lower than the concentrations listed above. We note in passing that to date no attempts have been made to speed up the reactions or explore the effects of obvious process variables such as quat to precursor ratio, overall reaction volume, and most importantly, temperature. Some of this work is ongoing.

3.2. SEM

Typical SEM micrographs are shown in Fig. 4. These cross-sectional micrographs of the FFs all reveal the 2D layered, structure of our flakes and the good stacking.

3.3.

Fig. 5a shows a TEM micrograph of QDB made with TMAH with a

Table 1 Diameters of quat cations, thickness of single MnO_2 slab and water used to estimate the interlayer distances shown in last column.

	Brock et al. (1999)		This work	
	Diameter (Å)	Interlayer Spacing (Å)	Diameter (Å)	Interlayer Spacing (Å)
ΓMA ⁺	6.0	9.0–9.6	5.6	9.4
TEA^+	6.5-7.5	17.0	6.7	9.4
TBA^+	9.5-10.5	16.6	8.3	12.1
MnO ₂ Slab	4.5		1.9	
Water	2.6		2.8	

lateral size ≈ 30 nm. The SAED image (inset in Fig. 5a) shows the presence of three sets of diffuse spots arranged in a hexagonal pattern.

In the QDB samples made with TBAH (Fig. 5b), the flakes were again ubiquitous in the TEM, albeit larger than the ones derived from TMAH. These flakes have a lateral size $\approx 0.1~\mu m$. The d-spacings of the first 3 rings are $\approx 2.5~\text{Å}, \approx 2~\text{Å}$ and $\approx 1.54~\text{Å}$ that are, respectively, ascribed to the $d_{100},~d_{102}$ and d_{110} spacings, of hexagonal birnessite. As discussed above, the 100 and 110 planes are observed in our XRD patterns and in our previous work, especially when the FF were held vertically with respect to the diffraction plane. The spacing of 2.0 Å was ascribed to the 102 planes to match those indexed by Drits et al. at 2.03 Å who showed that for single-layer birnessite, the 102 and 103 planes with d-spacings of 2.03 Å and 1.71 Å, respectively, are present in their XRD patterns [41]. Herein, we do not observe either of these peaks consistent with a turbostatic birnessite. The d-spacings of the last 2 rings, at 1.3 Å and 1.26 Å, remain unindexed.

Although, the figures shown here suggest mosaic 2D flakes, this is only one small view into the sample. In other areas, we observe large 2D flakes that appear single crystalline as can be seen in our previous work on QDB [23].

3.4. Raman spectroscopy

Raman spectra of the three QDB samples are plotted in Fig. 6. Like in our previous work, all peaks can be assigned to bending vibrations of the MnO_6 octahedra. These wavenumber peak values are slightly lower than those in the literature, but the overall spectral shape is consistent with that expected for a birnessite structure [21,22].

3.5. Zeta potential

The zeta potentials of the TMAH, TEAH and TBAH-derived samples were, respectively, -35 ± 2 mV, -35 ± 2 mV and -34 ± 1 mV. The fact that these values are so close together suggests that their surfaces are quite similar/comparable. Their relatively large values, on the other hand, explain why the colloids in water are stable for at least 6 months.

3.6. XPS

The XPS spectra of the Mn 2p and the oxygen (O) 1s regions are plotted in Fig. 7. The binding energies (BEs) of both Mn and O are similar between the three quats, similar to our previous work [23], and also to other published literature of TMA⁺ intercalated birnessite [42] with the Mn $2p_{3/2}$ peak centering at a BE of \approx 642.5 eV. The asymmetry of this peak, at the lower binding energies, is most likely due to other Mn oxide states [42,43], but XPS alone is not sufficient to determine the exact Mn oxidation state due to the large number of peaks needed to fit the envelopes shown in Fig. 7.

The O 1s spectra region matches with a metal-oxide bond at BEs of \approx 530 eV (red), a hydroxide bond at BE \approx 531 eV (blue), and organic O at BE of \approx 532 eV (green). These peaks are consistent with our previous work on quat-derived nanomaterials [22,23].

From the XPS spectra we can, however, obtain an atomic Mn:O ratio obtained from the areas of the Mn 2p 3/2 peak and the O peak at ≈ 530 eV. For TMA $^+$ QDB the ratio is $\sim\!1{:}2.7$, for TEA $^+$ the ratio is $\sim\!1{:}2.4$, and for TBA $^+$ the ratio is $\sim\!1{:}2.3$. Why these ratios are higher than one would expect for an MnO $_2$ based structure, is unclear at this time. The XPS results, however evident that Mn $^{4+}$ is the largest component. The most reasonable conclusion is that the extra O is adventitious, as these samples are not sputtered as it can cause issues with nanomaterials.

3.7. Gas sorption

Using the volume absorbed during gas sorption measurements (Fig. 8) we calculated the SSA of our powders using the BET equation. Samples made with TEAH resulted in the highest SSA of 67.6 m^2/g ,

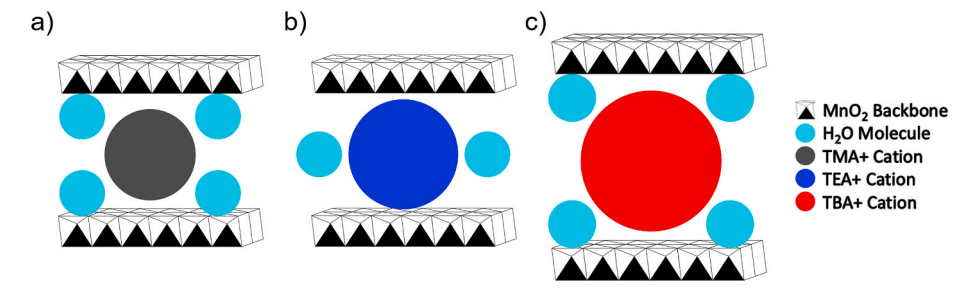


Fig. 3. Schematics of interlayer spacing of MnO₂ QDB made with, (a) TMAH, (b) TEAH, and (c) TBAH showing the cation, water, and MnO₂ layers.

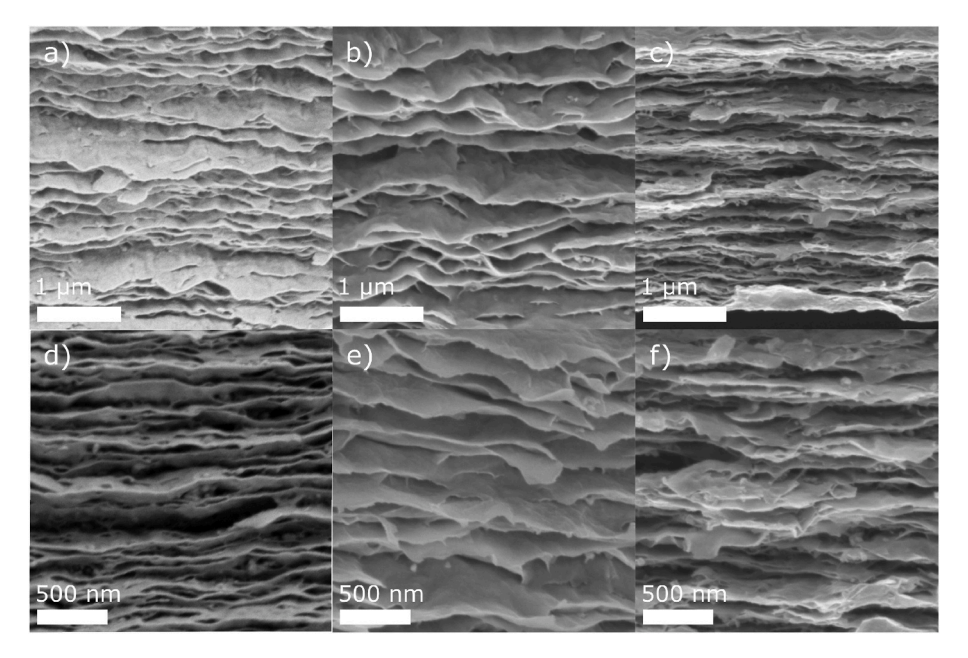


Fig. 4. SEM micrographs of QDB cross-sections of FFs made with, (a) TMAH, (b) TEAH, (c) TBAH. Micrographs (d, e, f) are higher magnification of (a, b, c) respectively.

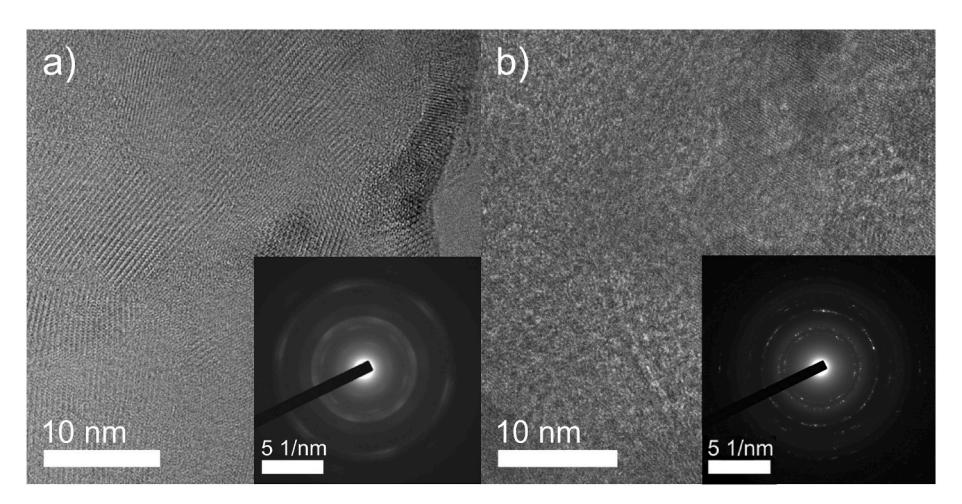


Fig. 5. TEM micrographs of Mn QDB made with, (a) TMAH, and (b) TBAH. Insets show SAED patterns of flakes imaged.

followed by TBAH with an SSA of $35.3~\text{m}^2/\text{g}$. At $15.2~\text{m}^2/\text{g}$, the TMAH samples had the lowest values. It is important to note that these values are far from a true representation of the actual SSA and only reflect the fact that the gas does not penetrate between the layers. This is quite common in 2D materials, such as MXenes [44].

3.8. UV-VIS

To determine the QDB band gap energies (Eg's) we used a UV–Vis spectrometer to measure the absorption of the samples suspended in DI water in quartz cuvettes in the 200–1000 nm wavelengths range. The insets in Fig. 9 show the collected absorption spectra for colloidal

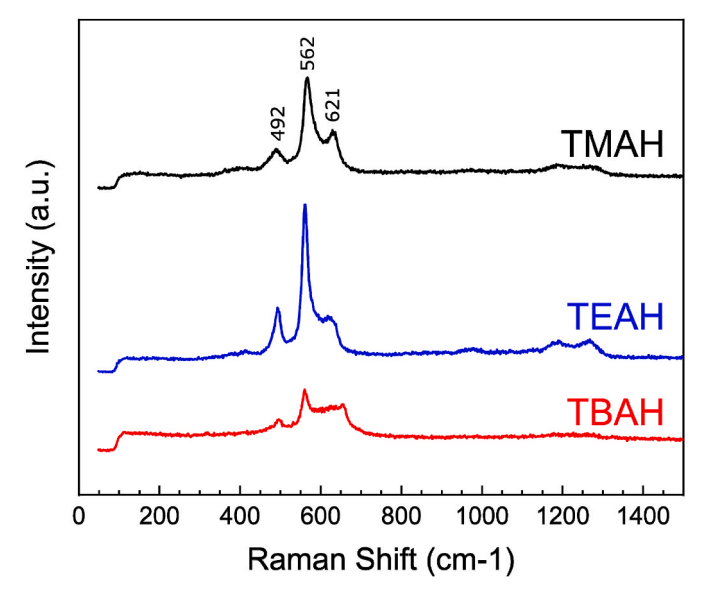


Fig. 6. Raman spectra of MnO_2 QDBs FFs made with TMAH (black), TEAH (blue), and TBAH (red). (For interpretation of the references to color in this figure legend, the reader is referred to the Web version of this article.)

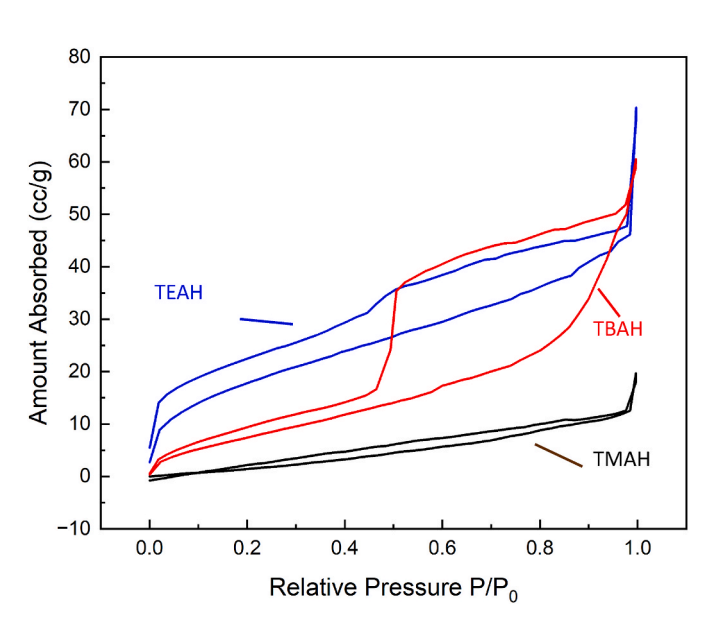


Fig. 8. Gas sorption of $\rm MnO_2$ QDB samples made with TMAH (black), TEAH (blue), and TBAH (red). (For interpretation of the references to color in this figure legend, the reader is referred to the Web version of this article.)

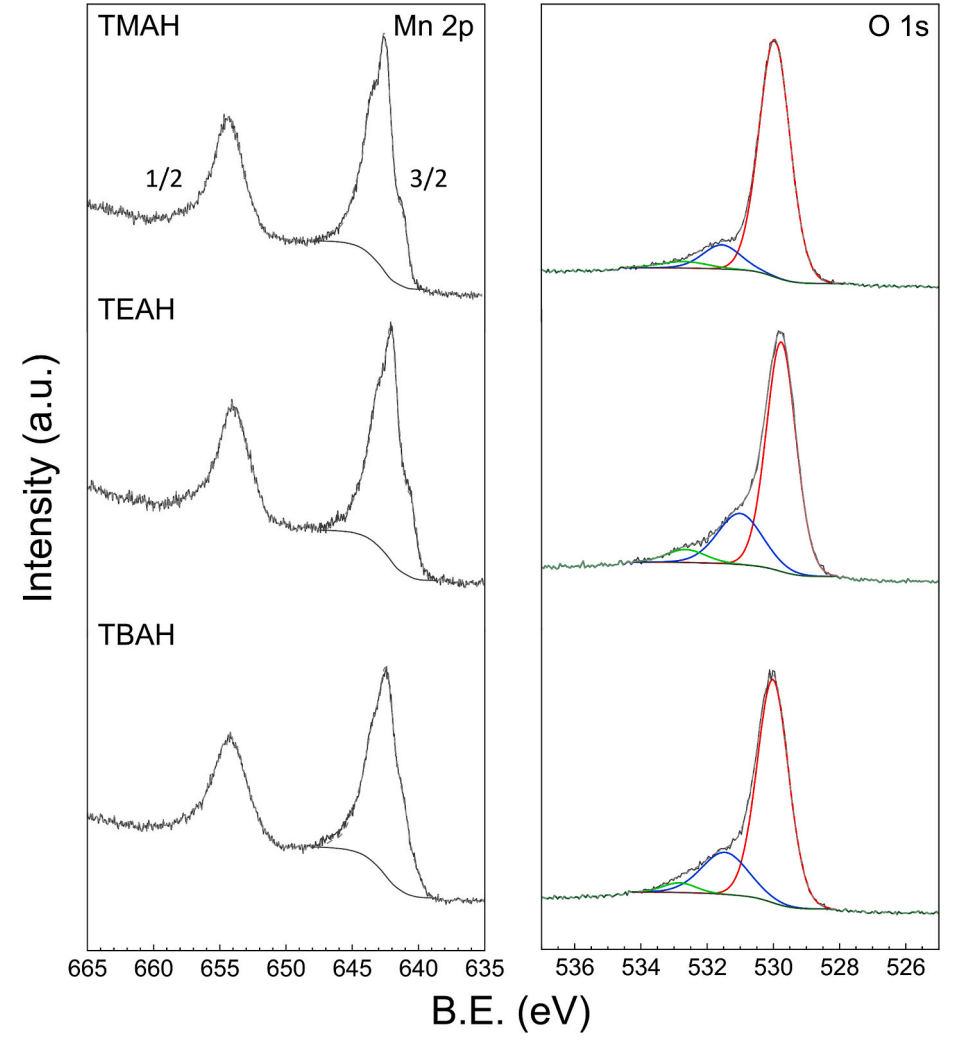
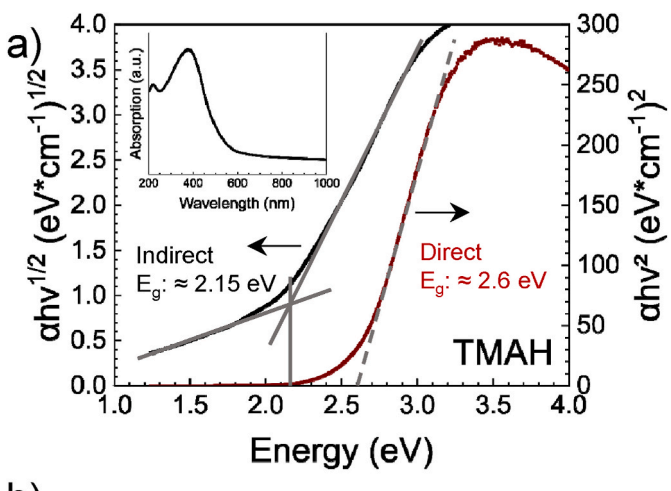
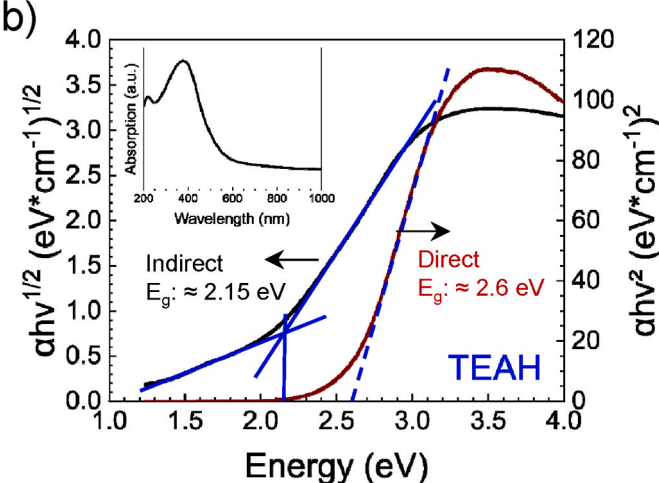


Fig. 7. XPS spectra of Mn 2p (left) and O 1s (right) for Mn QDB samples made with TMAH, TEAH, TBAH (top to bottom).





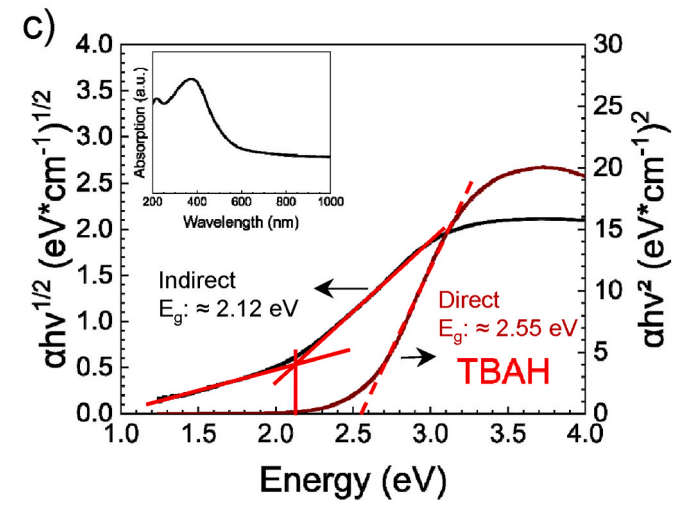


Fig. 9. Tauc plots of UV–vis absorption spectra (shown as insets) plotted as $\alpha h v^{1/2}$ (left y-axis) and $\alpha h v^2$ (right y-axis) for, (a) TMAH-, (b) TEAH-, (c) TBAH-derived samples. For all quats indirect E_g is ≈ 2.15 eV and direct E_g is ≈ 2.6 eV.

suspension samples made from TMAH (Fig. 9a inset), TEAH (Fig. 9b inset), and TEAH (Fig. 9c inset) in DI $\rm H_2O$ after subtracting the background. When these spectra were transformed into Tauc plots (Fig. 9) it is reasonable to conclude that all 3 materials possess indirect $\rm E_g$'s of ≈ 2.15 eV, as well as direct $\rm E_g$'s of ≈ 2.6 eV. In our previous work, we reported values of 2.46 eV and 2.64 eV, respectively [23]. These values are also in line with previous work on birnessite (2.1 eV and 2.2–2.7 eV) [45–47].

3.9. Oxygen Evolution Reaction (OER)

When the OER activities of the QDBs films made with the various quats in O_2 saturated 0.1 M KOH are compared (Fig. 10) they are comparable. When compared to our previous work [23], the activity here is slightly better. If anything, the OER activity appears to increase with the quat alkyl chain length. This comment notwithstanding, much work is needed before any hard conclusions can be reached.

4. Conclusions

Herein we present a simple method to synthesize crystalline, 2D birnessite starting with different quats. This one-pot, scalable method is almost fool-proof because all it entails is weighing the starting reactants, mixing them, and heating them at temperatures < 100 °C under ambient pressures. In our first report, we worked with TMAH. In this work, we not only reproduce our previous results but also show that TBAH and TEAH are equally effective and result in more or less the same material. At the Raman, TEM and SEM levels, the resulting flakes appear to quite similar and well-oriented parallel to the substrates. The similarities are also found with all 3 materials having matching indirect $E_{\rm g}$'s of \approx 2.15 eV, and direct $E_{\rm g}$'s of \approx 2.6 eV. Further, their OER activities are comparable.

The main difference, at the XRD level, is in the interlayer distance, d, that depends on the intercalated ion size. The spacings for the TMAH, TEAH and TBAH samples were ≈ 9.4 Å, ≈ 9.4 Å and ≈ 12.1 Å, respectively.

From a safety point of view, TBAH is safer than TMAH and would in principle be the quat used if our approach is commercialized. Of course, there are other considerations, but if safety is an issue, then TBAH could be used.

A possible impediment to commercialization is the time it takes for the reaction. The results shown here were not in any way optimized along these lines. The simplest method to speed up the reaction is to work at 95 $^{\circ}\text{C}$ instead of the 80 $^{\circ}\text{C}$ used here. Other important variables that need to be explored are the initial quat-to-Mn ratios, and overall reactant concentrations. Some of this work in ongoing, but hopefully others will be inspired by this work to further explore this quite promising approach for the scalable synthesis of nanomaterials, in general, and crystalline 2D birnessite flakes in particular.

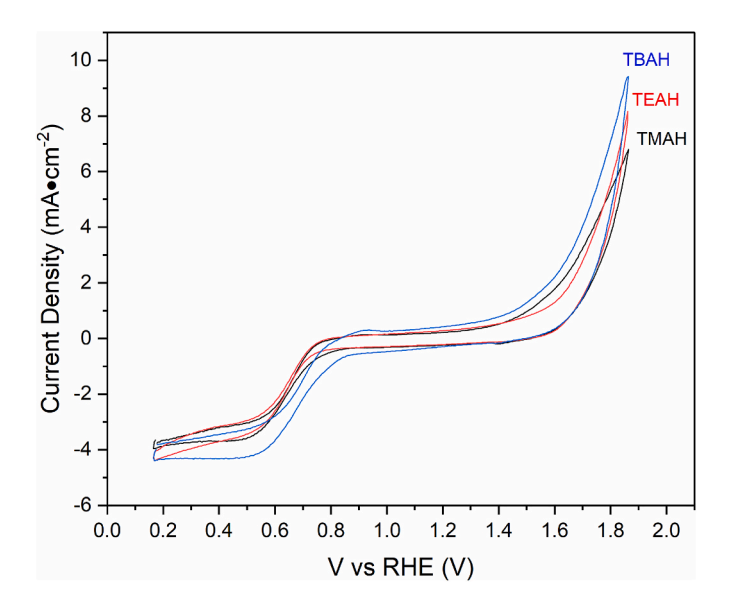


Fig. 10. OER polarization curves for TMAH QDB (black), TEAH QDB (red), and TBAH QDB (blue) in O_2 saturated 0.1 M KOH. (For interpretation of the references to color in this figure legend, the reader is referred to the Web version of this article.)

Funding

This work was supported by the Department of Education Graduate Assistance in Areas of National Need Grant, fund P200A180032; and NSF proposal number DMR-2211319.

Author contributions

M.Q.H., H.O.B. and M.W.B. conceived the idea and designed the experiments. M.Q.H. carried out synthesis all of the XRD, UV–Vis, XPS, and some of the SEM analysis and characterization. M.S.C. obtained some of the SEM micrographs. K.S. carried out the TEM-EDS characterization. T.K. carried out the Raman, gas sorption and zeta potential measurements. G.R.S. carried out the electrochemical measurement.

M.W.B. supervised the project assisted in the writing of the manuscript and secured the funding. All authors discussed the results and commented on the manuscript.

Declaration of competing interest

The authors declare that they have no known competing financial interests or personal relationships that could have appeared to influence the work reported in this paper.

Acknowledgements

XRD, SEM, TEM, and XPS analyses were performed using instruments in the Materials Characterization Core at Drexel University. We would like to thank Dr. Yuri Gogotsi for the use of the A.J. Drexel Nanomaterials Institute instruments to perform the Raman spectrometry, gas sorption and zeta potential measurements. We would also like to thank Dr. Joshua Snyder of Drexel University for the use of the electrochemical instruments.

References

- [1] S.L. Brock, M. Sanabria, S.L. Suib, V. Urban, P. Thiyagarajan, D.I. Potter, Particle size control and self-assembly processes in novel colloids of nanocrystalline manganese oxides, J. Phys. Chem. B 103 (1999) 7416–7428, https://doi.org/10.1021/jp991000u
- [2] M.M. Thackeray, C.S. Johnson, J.T. Vaughey, N. Li, S.A. Hackney, Advances in manganese-oxide 'composite' electrodes for lithium-ion batteries, J. Mater. Chem. 15 (2005) 2257, https://doi.org/10.1039/b417616m.
- [3] F.T. Ling, J.E. Post, P.J. Heaney, E.S. Ilton, The relationship between Mn oxidation state and structure in triclinic and hexagonal birnessites, Chem. Geol. 479 (2018) 216–227, https://doi.org/10.1016/j.chemgeo.2018.01.011.
- [4] B.J. Deibert, J. Zhang, P.F. Smith, K.W. Chapman, S. Rangan, D. Banerjee, K. Tan, H. Wang, N. Pasquale, F. Chen, K. Lee, G.C. Dismukes, Y.J. Chabal, J. Li, Surface and structural investigation of a MnO_x birnessite-type water oxidation catalyst formed under photocatalytic conditions, Chem. Eur J. 21 (2015) 14218–14228, https://doi.org/10.1002/chem.201501930.
- [5] J. Liu, L. Yu, E. Hu, B.S. Guiton, X.-Q. Yang, K. Page, Large-scale synthesis and comprehensive structure study of δ-MnO₂, Inorg. Chem. 57 (2018) 6873–6882, https://doi.org/10.1021/acs.inorgchem.8b00461.
- [6] Q. Gao, O. Giraldo, W. Tong, S.L. Suib, Preparation of nanometer-sized manganese oxides by intercalation of organic ammonium ions in synthetic birnessite OL-1, Chem. Mater. 13 (2001) 778–786, https://doi.org/10.1021/cm000426c.
- [7] D.G. Beak, N.T. Basta, K.G. Scheckel, S.J. Traina, Linking solid phase speciation of Pb sequestered to birnessite to oral Pb bioaccessibility: implications for soil remediation, Environ. Sci. Technol. 42 (2008) 779–785, https://doi.org/10.1021/ es/71.733n
- [8] B. Ding, P. Zheng, P. Ma, J. Lin, Manganese oxide nanomaterials: synthesis, properties, and theranostic applications, Adv. Mater. 32 (2020), 1905823, https://doi.org/10.1002/adma.201905823.
- [9] R.M. McKenzie, The synthesis of birnessite, cryptomelane, and some other oxides and hydroxides of manganese, Mineral. Mag. 38 (1971) 493–502, https://doi.org/ 10.1180/minmag.1971.038.296.12.
- [10] L.H.P. Jones, A.A. Milne, Birnessite, a new manganese oxide mineral from Aberdeenshire, Scotland, Mineral. Mag. 31 (1956) 283–288, https://doi.org/ 10.1180/minmag.1956.031.235.01.
- [11] Q. Feng, K. Yanagisawa, N. Yamasaki, Synthesis of birnessite-type potassium manganese oxide, J. Mater. Sci. Lett. 16 (1997) 110–112, https://doi.org/10.1023/ A:1018577523676.
- [12] D. Frías, S. Nousir, I. Barrio, M. Montes, T. López, M.A. Centeno, J.A. Odriozola, Synthesis and characterization of cryptomelane- and birnessite-type oxides:

- precursor effect, Mater. Char. 58 (2007) 776–781, https://doi.org/10.1016/j.
- [13] S. Hirano, R. Narita, S. Naka, Hydrothermal synthesis and properties of $Na_{0.70}MnO_{2.25}$ layer crysta, Mater. Res. Bull. 19 (1984) 1229–1235, https://doi.org/10.1016/0025-5408(84)90076-X.
- [14] K. Kai, Y. Yoshida, H. Kageyama, G. Saito, T. Ishigaki, Y. Furukawa, J. Kawamata, Room-temperature synthesis of manganese oxide monosheets, J. Am. Chem. Soc. 130 (2008) 15938–15943, https://doi.org/10.1021/ja804503f.
- [15] Y. Omomo, T. Sasaki, Wang, M. Watanabe, Redoxable nanosheet crystallites of MnO₂ derived via delamination of a layered manganese oxide, J. Am. Chem. Soc. 125 (2003) 3568–3575, https://doi.org/10.1021/ja021364p.
- [16] Z. Liu, K. Ooi, H. Kanoh, W. Tang, T. Tomida, Swelling and delamination behaviors of birnessite-type manganese oxide by intercalation of tetraalkylammonium ions, Langmuir 16 (2000) 4154–4164, https://doi.org/10.1021/la9913755.
- [17] N. Sakai, K. Fukuda, Y. Omomo, Y. Ebina, K. Takada, T. Sasaki, Heteronanostructured films of titanium and manganese oxide nanosheets: photoinduced charge transfer and electrochemical properties, J. Phys. Chem. C 112 (2008) 5197–5202, https://doi.org/10.1021/jp7119894.
- [18] N. Sakai, K. Fukuda, R. Ma, T. Sasaki, Synthesis and substitution chemistry of redox-active manganese/cobalt oxide nanosheets, Chem. Mater. 30 (2018) 1517–1523, https://doi.org/10.1021/acs.chemmater.7b04068.
- [19] R. Borgohain, J.P. Selegue, Y.-T. Cheng, Ternary composites of delaminated-MnO₂/PDDA/functionalized-CNOs for high-capacity supercapacitor electrodes, J. Mater. Chem. A. 2 (2014) 20367–20373, https://doi.org/10.1039/C4TA04439H.
- [20] P. Gao, P. Metz, T. Hey, Y. Gong, D. Liu, D.D. Edwards, J.Y. Howe, R. Huang, S. T. Misture, The critical role of point defects in improving the specific capacitance of δ-MnO₂ nanosheets, Nat. Commun. 8 (2017), 14559, https://doi.org/10.1038/ncomms14559.
- [21] H.O. Badr, F. Lagunas, D.E. Autrey, J. Cope, T. Kono, T. Torita, R.F. Klie, Y.-J. Hu, M.W. Barsoum, On the structure of one-dimensional TiO₂ lepidocrocite, Matter 6 (2022) 128–141, https://doi.org/10.1016/j.matt.2022.10.015.
- [22] H.O. Badr, T. El-Melegy, M. Carey, V. Natu, M.Q. Hassig, C. Johnson, Q. Qian, C. Y. Li, K. Kushnir, E. Colin-Ulloa, L.V. Titova, J.L. Martin, R.L. Grimm, R. Pai, V. Kalra, A. Karmakar, A. Ruffino, S. Masiuk, K. Liang, M. Naguib, O. Wilson, A. Magenau, K. Montazeri, Y. Zhu, H. Cheng, T. Torita, M. Koyanagi, A. Yanagimachi, T. Ouisse, M. Barbier, F. Wilhelm, A. Rogalev, J. Björk, P.O. Å. Persson, J. Rosen, Y.-J. Hu, M.W. Barsoum, Bottom-up, scalable synthesis of anatase nanofilament-based two-dimensional titanium carbo-oxide flakes, Mater. Today 54 (2022) 8–17, https://doi.org/10.1016/j.mattod.2021.10.033.
- [23] H.O. Badr, K. Montazeri, T. El-Melegy, V. Natu, M. Carey, R. Gawas, P. Phan, Q. Qian, C.Y. Li, U. Wiedwald, M. Farle, E. Colin-Ulloa, L.V. Titova, M. Currie, T. Ouisse, M. Barbier, A. Rogalev, F. Wilhelm, M. Hans, J.M. Schneider, C. Tandoc, Y.-J. Hu, J. Snyder, M.W. Barsoum, Scalable, inexpensive, one-pot, facile synthesis of crystalline two-dimensional birnessite flakes, Matter 5 (2022) 2365–2381, https://doi.org/10.1016/j.matt.2022.05.038.
- [24] M. Ghaly, F.M.S.E. El-Dars, M.M. Hegazy, R.O. Abdel Rahman, Evaluation of synthetic Birnessite utilization as a sorbent for cobalt and strontium removal from aqueous solution, Chem. Eng. J. 284 (2016) 1373–1385, https://doi.org/10.1016/ i.cei.2015.09.025.
- [25] P. Tang, W. Huang, D. Wang, Z. Liu, J. Wang, 2D layered K-birnessite MnO₂-based photocatalytic membrane for catalytic filtration degradation of organic pollutants, Water Air Soil Pollut. 234 (2023) 120, https://doi.org/10.1007/s11270-023-06133-x
- [26] Y. Luo, W. Tan, S.L. Suib, G. Qiu, F. Liu, Dissolution and phase transformation processes of hausmannite in acidic aqueous systems under anoxic conditions, Chem. Geol. 487 (2018) 54–62, https://doi.org/10.1016/j.chemgeo.2018.04.016.
- [27] D.F. Hewett, Manganite, hausmannite, braunite; features, modes of origin, Econ. Geol. 67 (1972) 83–102, https://doi.org/10.2113/gsecongeo.67.1.83.
- [28] A.A. Yadav, S.N. Jadhav, D.M. Chougule, P.D. Patil, U.J. Chavan, Y.D. Kolekar, Spray deposited Hausmannite Mn₃O₄ thin films using aqueous/organic solvent mixture for supercapacitor applications, Electrochim. Acta 206 (2016) 134–142, https://doi.org/10.1016/j.electacta.2016.04.096.
- [29] Sigma-Aldrich Inc., Tetramethylammonium Hydroxide Solution, 2021. St. Louis.
- [30] Thermo Fisher Scientific Chemicals Inc., Tetramethylammonium Hydroxide, 25% W/w Aqueous Solution, Ward Hill, Electronic Grade, 2010.
- [31] Sigma-Aldrich Inc., Tetrabutylammonium Hydroxide Solution, 2021. St. Louis.
- [32] Fisher Scientific UK, Tetra-n-butylammonium Hydroxide \sim 40% Solution, Leicestershire, 2021.
- [33] R. Zhao, L. Zhang, C. Wang, L. Yin, Tetramethylammonium cation intercalated layered birnessite manganese dioxide for high-performance intercalation pseudocapacitor, J. Power Sources 353 (2017) 77–84, https://doi.org/10.1016/j. ipowsour.2017.03.138.
- [34] X. Yang, Y. Makita, Z. Liu, K. Sakane, K. Ooi, Structural characterization of self-assembled MnO₂ nanosheets from birnessite manganese oxide single crystals, Chem. Mater. 16 (2004) 5581–5588, https://doi.org/10.1021/cm049025d.
- [35] M. Nakayama, S. Konishi, H. Tagashira, K. Ogura, Electrochemical synthesis of layered manganese oxides intercalated with tetraalkylammonium ions, Langmuir 21 (2005) 354–359, https://doi.org/10.1021/la048173f.
- [36] J. Luo, S.L. Suib, Formation and transformation of mesoporous and layered manganese oxides in the presence of long-chain ammonium hydroxides, Chem. Commun. (1997) 1031–1032, https://doi.org/10.1039/a701690e.
- [37] S. Kubota, S. Ozaki, J. Onishi, K. Kano, O. Shirai, Selectivity on ion transport across bilayer lipid membranes in the presence of gramicidin A, Anal. Sci. 25 (2009) 189–193, https://doi.org/10.2116/analsci.25.189.

- [38] Y. Marcus, Thermodynamics of solvation of ions. Part 5.—Gibbs free energy of hydration at 298.15 K, J. Chem. Soc., Faraday Trans. 87 (1991) 2995–2999, https://doi.org/10.1039/FT9918702995.
- [39] J.S. D'Arrigo, Screening of membrane surface charges by divalent cations: an atomic representation, Am. J. Physiol. Cell Physiol. 235 (1978) C109–C117, https://doi.org/10.1152/ajpcell.1978.235.3.C109.
- [40] Paul Kebarle, S.K. Searles, A. Zolla, J. Scarborough, M. Arshadi, Solvation of the hydrogen ion by water molecules in the gas phase. Heats and entropies of solvation of individual reactions. H+(H₂O)_{n-1} + H₂O .fwdarw. H⁺(H₂O)_n, J. Am. Chem. Soc. 89 (1967) 6393–6399, https://doi.org/10.1021/ja01001a001.
- [41] V.A. Drits, E. Silvester, A.I. Gorshkov, A. Manceau, Structure of synthetic monoclinic Na-rich birnessite and hexagonal birnessite: I, Results from X-ray diffraction and selected-area electron diffraction, Am. Mineral. 82 (1997) 946–961, https://doi.org/10.2138/am-1997-9-1012.
- [42] R. Zhao, L. Zhang, C. Wang, L. Yin, Tetramethylammonium cation intercalated layered birnessite manganese dioxide for high-performance intercalation pseudocapacitor, J. Power Sources 353 (2017) 77–84, https://doi.org/10.1016/j. jpowsour.2017.03.138.
- [43] X. Sun, V. Duffort, B.L. Mehdi, N.D. Browning, L.F. Nazar, Investigation of the mechanism of Mg insertion in birnessite in nonaqueous and aqueous rechargeable

- Mg-ion batteries, Chem. Mater. 28 (2016) 534–542, https://doi.org/10.1021/acs.chemmater.5b03083
- [44] Y. Dall'Agnese, P. Rozier, P.-L. Taberna, Y. Gogotsi, P. Simon, Capacitance of twodimensional titanium carbide (MXene) and MXene/carbon nanotube composites in organic electrolytes, J. Power Sources 306 (2016) 510–515, https://doi.org/ 10.1016/j.jpowsour.2015.12.036.
- [45] G. Ren, M. Sun, Y. Sun, Y. Li, C. Wang, A. Lu, H. Ding, A cost-effective birnessite-silicon solar cell hybrid system with enhanced performance for dye decolorization, RSC Adv. 7 (2017) 47975–47982, https://doi.org/10.1039/ C7RA08468D.
- [46] G. Ren, Y. Sun, Y. Ding, A. Lu, Y. Li, C. Wang, H. Ding, Enhancing extracellular electron transfer between Pseudomonas aeruginosa PAO1 and light driven semiconducting birnessite, Bioelectrochemistry 123 (2018) 233–240, https://doi. org/10.1016/j.bioelechem.2018.06.003.
- [47] B.A. Pinaud, Z. Chen, D.N. Abram, T.F. Jaramillo, Thin films of sodium birnessite-type MnO₂: optical properties, electronic band structure, and solar photoelectrochemistry, J. Phys. Chem. C 115 (2011) 11830–11838, https://doi.org/10.1021/jp200015p.